Endothermic Reaction at Room Temperature enabled by Deep-Ultraviolet Plasmons

Canhui Wang[1,2], Wei-Chang D. Yang[1,2#], David Raciti[3], Alina Bruma[1,2], Ronald Marx[4], Amit Agrawal[1,2], and Renu Sharma[1*]

1. Physical Measurement Laboratory, National Institute of Standards and Technology, Gaithersburg, MD 20899, USA.

2. Institute for Research in Electronics and Applied Physics & Maryland NanoCenter, University of Maryland, College Park, MD 20742, USA.

3. Measurement and Materials Laboratory, National Institute of Standards and Technology, Gaithersburg, MD 20899, USA.

4. DENSsolutions B.V., Delft 2628 ZD, The Netherlands.

* Correspondence to: renu.sharma@nist.gov

Secondary Corresponding Author: david.yang@nist.gov

Metallic nanoparticles have been used to harvest energy from a light source and transfer it to adsorbed gas molecules resulting in reduced chemical reaction temperature. However, most reactions reported, such as ethylene epoxidation, ammonia decomposition, and H-D bond formation, are exothermic and only H-D bond formation has been achieved at room temperature. These reactions require low activation energies (< 2 eV), which are readily attained using visible frequency localized surface plasmons (from ≈ 1.75 eV to ≈ 3.1 eV). Here, we show that endothermic reactions requiring higher activation energy (> 3.1 eV) can be initiated at room temperature using localized surface plasmons in the deep-UV range. As an example, by leveraging simultaneous excitation of multiple localized surface plasmon (LSP) modes of Al nanoparticles using high-energy electrons, we initiate reduction of CO_2 to CO by carbon, at room temperature. We employ an environmental transmission electron microscope to excite and characterize Al LSP resonances, and simultaneously measure the spatial distribution of carbon gasification near the nanoparticles in a CO_2 environment. This approach opens a path towards exploring other industrially relevant chemical processes initiated by plasmonic fields at room temperature.

Plasmonic nanoparticles have been shown to harvest energy from a photon source to drive chemical reactions at lower temperatures and/or higher rate, mimicking photocatalysis[1]. It has been proposed that the localized surface plasmons (LSP), generated by the resonant excitation of free surface valence electrons of certain metal nanoparticles, such as Au, Ag, Cu or Al, is responsible for driving low temperature reactions during the dephasing process[2-6]. Indirect photocatalysis, where the photon energy harvested by plasmonic particles is transferred to a nearby semiconductor to create high energy electron-hole pairs to drive endothermic reactions such as water splitting and CO_2 conversion, have been studied extensively[7-12]. Recently direct photocatalysis, where LSP energy is directly transferred to adsorbed reactants on a metal nanoparticle surface, has also been employed to overcome or reduce the activation energy barrier for various chemical reactions, such as ethylene epoxidation[2], H-D bond formation[4], ammonia decomposition[13], by compensating for the otherwise needed thermal energy[14,15]. Moreover, electron beam excited LSP resonance energy of Au nanoprisms has recently been reported to initiate room temperature CO disproportionation, generally known as the Boudouard reaction ($2CO_{(g)} \rightarrow CO_{2(g)} + C_{(s)}$)[16]. This reaction is of particular interest as the reverse reaction ($CO_{2(g)} + C_{(s)} \rightarrow 2CO_{(g)}$) may provide an alternative path for CO_2 reduction. Without LSP resonance energy, the CO disproportionation reaction is reported to occur at temperatures between 400 °C to 600 °C and reverses as the temperature is increased above 700 °C.[17] Also, the activation energy of the reverse Boudouard reaction has been reported to be between 2.91 eV and 3.9 eV[18,19]. Therefore, Al nanoparticles with multimode LSP resonance energies spanning from the visible to the deep-ultraviolet, approximately between 2 eV and 8 eV[20,21], can be used as a route for CO_2 reduction by carbon. Moreover, Al is readily available and cheaper than noble metals, making it a potential candidate for channeling energy from light to perform large scale CO_2 reduction. We tested our hypothesis by leveraging an electron beam to

simultaneously excite the various LSP modes of Al nanoparticles in an environmental scanning transmission electron microscope (ESTEM), operated at 80 kV and equipped with a monochromated electron source (80 meV energy resolution). We characterized the spatial distribution of LSP modes using electron energy-loss spectroscopy (EELS) and measured the resulting carbon gasification near the nanoparticles in a CO_2 environment to estimate the reaction rate. Finally, to support this hypothesis, *in situ* gas chromatograph-mass spectrometer (GCMS) measurements during electron beam illumination were utilized to directly detect CO as a reaction product. Simultaneous excitation of various modes on Al nanoparticles by high energy electrons mitigates the need for a broadband photon source extending into the deep-UV to investigate LSP induced reactions. Moreover, ESTEM enables the spatial distribution of LSP modes and the dynamic behavior of the plasmonic nanoparticles to be characterized simultaneously.

Suspensions of Al nanoparticles and graphite flakes, loaded on lacey carbon TEM grids, were introduced in the ESTEM column (see Methods). Representative annular dark-field (ADF) images, acquired in the STEM mode, of an Al nanoparticle attached to graphite are shown in Fig. 1a and Extended Data Fig. 1a. Core-loss EELS maps of the nanoparticle, acquired using L-edges of Al, and K-edges of O and C (Extended Data Fig. 1b), reveal a core-shell structure with an Al core (Al map, Extended Data Fig. 1c) surrounded by an Al_2O_3 shell ($\approx$ 4 nm thick) as indicated by the oxygen map (Extended Data Fig. 1d). Carbon is limited to the graphite support region (Extended Data Fig. 1e) and the overall elemental distribution is shown in Extended Data Fig. 1f. LSP resonances were excited using an electron beam ($\approx$ 1 nm diameter) positioned $\approx$ 2 nm away from the surface of the nanoparticle (magenta dot, Fig. 1a). A low-loss EELS response with multiple peaks representing the various LSP resonance modes and the electrostatic plasmon mode is shown

in Fig. 1b, black curve[22]. Our rigorous modeling and analysis suggest that the energy-loss peak of highest intensity located at 7.280 eV ± 0.003 eV (error represents one standard deviation of Gaussian profile fitting) is a broad feature that, given their proximity, contains both a high order resonance mode and an electrostatic mode. For EELS acquired using the electron beam positioned outside nanoparticles of different diameters (aloof-mode), the LSP resonance modes are always located at lower energies than the electrostatic mode and tend to redshift for larger nanoparticle diameters (Extended Data Fig. 2). The elemental distribution of the nanoparticle was used to build a meshed three-dimensional (3D) model (Fig. 1c) for the metallic nanoparticles boundary element method (MNPBEM) simulations[23] (see Methods). Simulated EELS spectral features (Fig. 1b, blue curve) for the polarization of charges on the nanoparticle surface match reasonably well with the experimental data, except that the full width at half maxima of the measured ≈ 7.28 eV peak is slightly broader. The spectral peaks, centered at ≈ 2.95 eV and ≈ 5.45 eV, corresponding to the dipole and quadrupole LSP modes of the nanoparticle, can also be identified by comparing the measured EELS to the simulated loss probability (Fig. 1b)[24]. The peak energies of the resonance modes are associated with the nanoparticle size, whereas that of the electrostatic is governed by the Al/Al_2O_3 interface. As we learn from the simulated electron energy-loss probability for nanoparticles of different diameters (Extended Data Fig. 3), for a larger nanoparticle, an increase in surface area (assuming a constant Al_2O_3 shell thickness) results in longer wavelengths for the LSP resonances, and sustains high order resonance modes, such as a hexapole mode for the nanoparticle shown in Fig. 1a.

These observations are further confirmed using numerical calculations based on the Mie scattering theory and rigorous fully three-dimensional electromagnetic simulations based on the

Discontinuous Galerkin Time-Domain (DGTD) method[25]. The extinction spectra calculated using the Mie theory for Al nanoparticles with diameters ranging from 50 nm to 150 nm (coated with a 4 nm thick Al_2O_3 shell) clearly shows the evolution of various LSP modes (Extended Data Fig. 4) that are consistent in trend with the experimental results (Extended Data Fig. 2) and MNPBEM calculations (Extended Data Fig. 3). Noticeably, for a nanoparticle of 100 nm diameter, the three peaks in the extinction spectra correspond to the dipole, quadrupole and hexapole modes with their corresponding field distributions, calculated using the DGTD technique, shown in Extended Data Fig. 5. The discrepancy in the precise location of these peaks can simply be attributed to the presence of graphite in the proximity of the Al nanoparticle in experiments causing further redshifts in the observed peaks. Note that the broad peak in the experiments at ≈ 7.28 eV consists of both a higher order plasmon mode and the electrostatic plasmon mode.

Spatial distribution of the electric field near the Al nanoparticle and graphite interface (circled by the green, dashed box in Fig. 1c) was simulated using MNPBEM by placing the electron beam ≈ 2 nm away from the surface of the Al nanoparticle (marked by the magenta point in Fig. 1c). The simulated electric field amplitude map associated with the hexapole mode at ≈ 7.28 eV (Fig. 1d) clearly illustrates that the induced electric field is distributed on the side of nanoparticle in contact with the graphite. The evanescent field amplitude gradients (Fig. 1e) into the graphite (in the direction of the arrow in Fig. 1d), resulting from the LSP resonance dipole mode (≈ 2.95 eV), quadrupole mode (≈ 5.45 eV) and hexapole mode (≈ 7.28 eV), indicates the possibility of using the LSP resonance mode energies to initiate the local reaction between CO_2 and carbon when the electron beam is positioned at the far side of the nanoparticle. The spatial range of the local reaction

is then presumably affected by the decay length of the evanescent fields, the estimation of which is provided in the Supplementary Information.

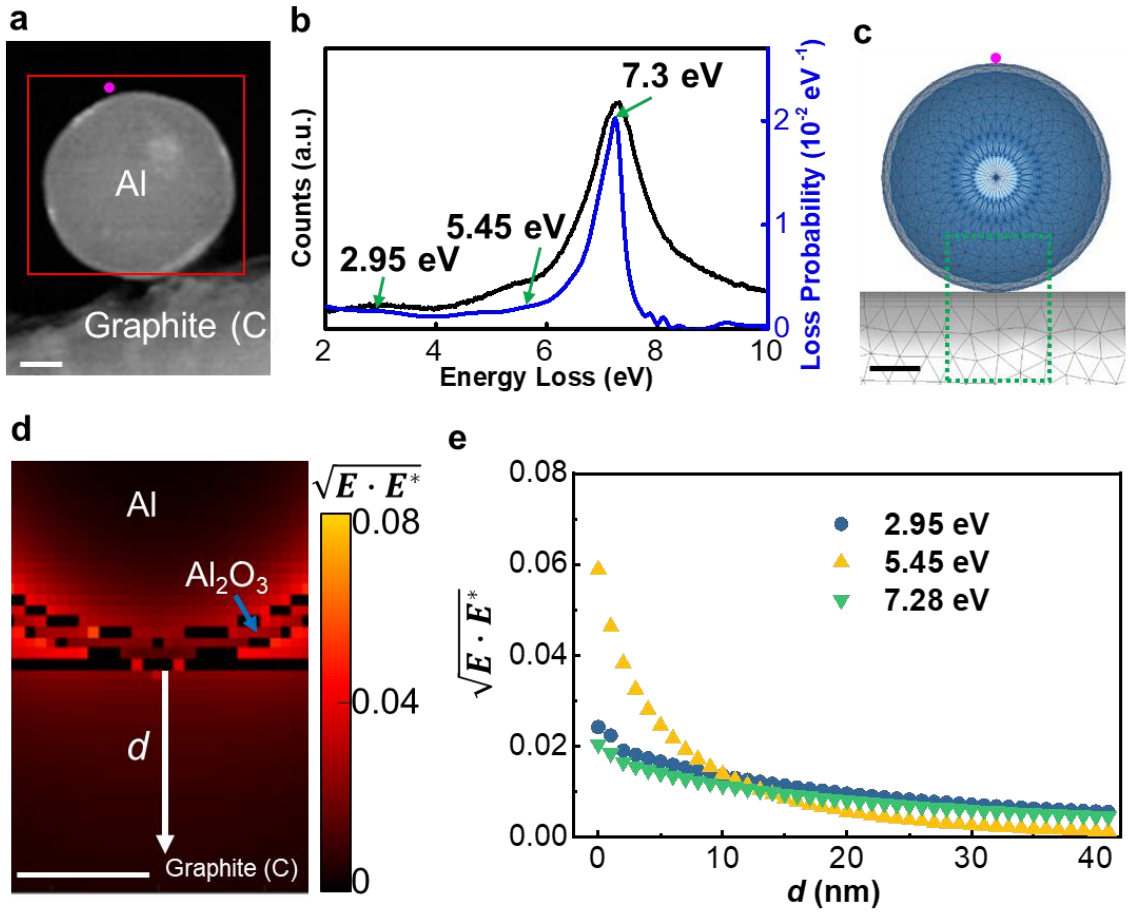

Fig. 1 | Electric field distribution of electron beam excited LSP resonance. a, ADF image showing an Al nanoparticle attached to a graphite flake. The magenta dot and red square show the location of the electron beam and the area, used for the acquisition of EELS spectrum and an EELS map, respectively. **b,** Experimental (black line) and simulated (blue line) energy-loss probability from the electron beam placed at the magenta dot in **a** and **c**, respectively. **c,** A 3D model constructed based on the Al, O and C distribution in **a** (Extended Data Fig. 1, **c**-**f**). The green dotted square and the magenta dot indicate the area from where the electric field distribution is simulated and the location of the electron beam, respectively. **d,** Electric field distribution of the area indicated by the green dashed square in **c**, simulated using the MNPBEM toolbox at 7.3 eV, with the electron beam placed at magenta dot shown in **c**. **e,** Blue, yellow and green line profiles show electric field amplitude for 2.95 eV, 5.45 eV and 7.3 eV, respectively, in graphite as a function of distance away from the Al nanoparticle, extracted from the location and direction indicated by the white arrow in **d**. The scale bars are 25 nm.

Experiments were performed in a controlled CO_2 environment using the Al-graphite configuration as shown in Fig. 2a with the electron beam in the aloof mode. The nanoparticle is partially attached to the graphite flake on lacey carbon support (Fig. 2b), and an aloof mode was chosen to mitigate the possibility of direct interaction of the electron beam with either Al or graphite. We introduced CO_2 at a partial pressure of ≈ 50 Pa with the electron beam (magenta dot, Fig. 2b) placed ≈ 6 nm away from the surface of the Al nanoparticle (dotted red line, Fig. 2b). The beam position was chosen to ensure that it stays in aloof mode for the duration of the experiment (see Methods). After ≈ 150 min of continuous exposure, the recession of carbon/graphite boundary with respect to the original position, marked by a blue dashed line in the ADF image (Fig. 2c) confirms the etching of both the lacey carbon support and graphite. The Al nanoparticle was also observed to move with the receding graphite edge as it continues to stay in contact with it. The distance between the nanoparticle edge and electron beam position increased at the rate of ≈ 0.173 $nm \cdot min^{-1}$ finally reaching ≈ 32 nm after 150 minutes. We expect that after ≈ 150 minutes the electric field amplitude is too weak to continue the reaction.

The relative etching rate of graphite was monitored by acquiring spectrum images in the STEM mode (see Supplementary Information): both in vacuum, one before the reaction (V_i, Fig. 2d) and the other after the reaction post-evacuation of CO_2 (V_f, Fig. 2e). Two separate t/λ maps were extracted from the spectrum images, where t is the thickness of the material and λ is the inelastic mean free path (MFP) defined as the average distance traveled by an electron between successive collisions in a constituent material. The line profile of carbon thickness, up to ≈130 nm from the surface of the Al nanoparticle into the graphite, averaged over 5 pixels, was measured from the areas marked as 1 (Fig. 2d) and 2 (Fig. 2e). The carbon etching profile (curve 3, Fig. 2f) was

obtained by subtracting the measured thickness after the reaction (curve 2, Fig. 2f), from the one acquired before the reaction (curve 1, Fig. 2f). The etch profile (curve 3) clearly shows a decrease in etching of graphite away from the nanoparticle surface, reducing to nearly zero at ≈ 100 nm. The largest reduction in graphite thickness is at the nanoparticle surface and decreases away from it. This is consistent with the decay of the electric field (Fig. 1e), indicating that the electric field associated with the LSP mode at the interface where Al nanoparticle is in contact with graphite, is causing the carbon etching in the presence of CO_2[26].

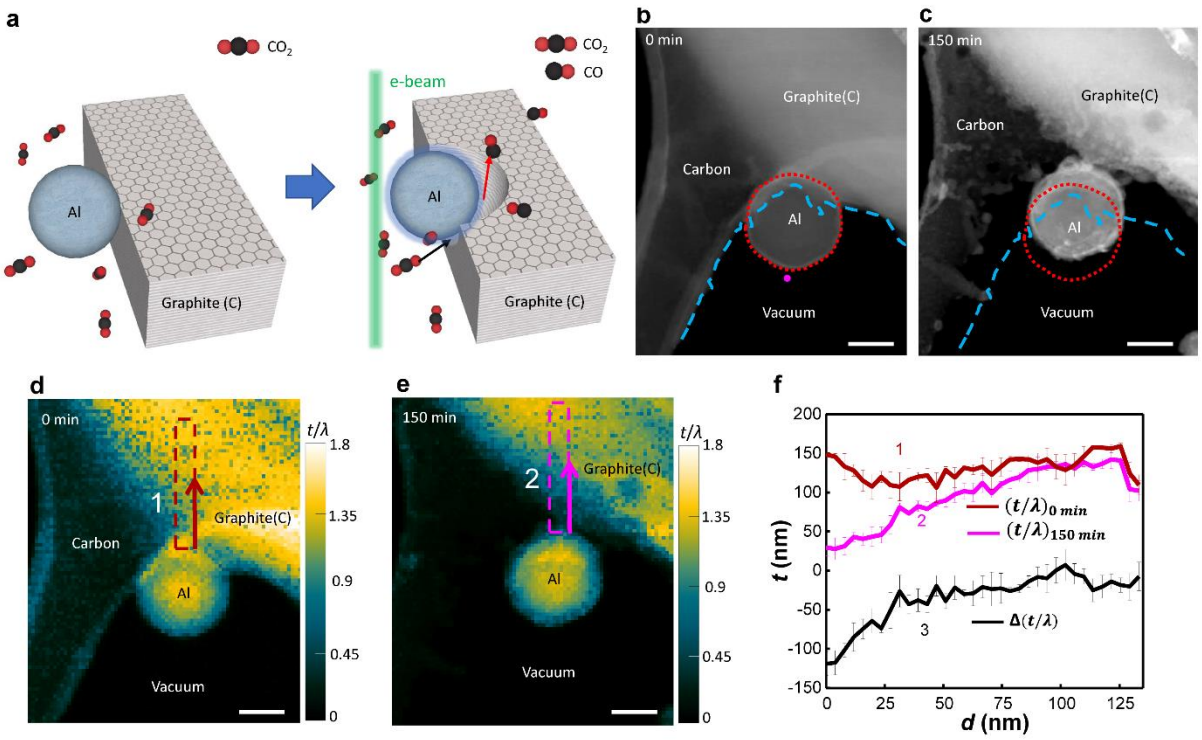

Fig. 2 | Carbon etching with the aloof electron beam. a, A schematic showing the desired configuration of an Al nanoparticle and a graphite flake and the expected carbon etching volume around the nanoparticle. **b,** ADF image showing an Al nanoparticle attached to graphite and lacey carbon film in vacuum. The magenta dot shows the drift corrected position of the electron beam with a beam current of ≈ 1.5 nA (equivalent flux ≈ 0.12 nA·nm^{-2}), ≈ 6 nm away from the nanoparticle surface, (see Methods). **c,** ADF image of the same region after the electron beam excitation for ≈ 150 min in CO_2 at a partial pressure of ≈ 50 Pa, recorded after evacuating the CO_2 from the sample area. The red dotted and blue dashed lines in **b** and **c** represent the outline of the Al nanoparticle and the carbon, respectively, at the beginning of the reaction. **d-e,** t/λ maps (see Supplementary Information) showing the thickness distribution in the area shown in **b** and **c**,

respectively. **f,** Line profiles acquired from the locations marked (dashed rectangles 1 and 2, the direction indicated by a red and magenta arrow, respectively) in **d** and **e**. Line profiles are averaged in the direction perpendicular to the red and magenta arrows with a width of 5 pixels. Error is one standard deviation of 5 measurements from each pixel. Line 3 is the sample thickness change obtained by subtracting values in line 1 from line 2. The scale bars are 50 nm.

For the LSP driven reduction of CO_2 with the electron beam in the aloof-mode, the average measured carbon etching rate of ≈ 0.222 $nm \cdot min^{-1}$, appears to be low (see Supplementary Information) for practical applications. The low etching rate can be attributed to the weak electric field amplitude associated with the LSP mode at the nanoparticle-graphite interface when using the aloof mode excitation (Fig. 1, d-e). In contrast, for parallel beam excitation, mimicking the case of unpolarized photon excitation, the induced plasmonic field is expected to be distributed over the entire nanoparticle surface, driven by the passing swift electrons within the parallel beam. This configuration should therefore result in a concurrent increase in the reaction volume for Al nanoparticles loaded on graphite leading to a higher etching rate (Fig. 3, a-b). An example of a single Al nanoparticle continuously etching graphite away under *in situ* TEM observation in a CO_2 environment at a partial pressure of ≈ 50 Pa is shown in Extended Data Movie 1. Time resolved TEM images of multiple Al nanoparticles located at the edge of graphitic flake, acquired using parallel beam illumination, further illustrate the graphite etching process (Fig. 3c). Red dotted and blue dashed lines mark the initial positions of the nanoparticles and the edge of graphite flake, respectively (Fig. 3c). Subsequently, a new receded edge of the graphite flake (yellow dotted line, Fig. 3d) formed after ≈ 7 min of electron beam excitation at a flux of ≈ 9.1×10^{-6} $nA \cdot nm^{-2}$. Note that the nanoparticles also moved (original position marked by red dotted line in Fig. 3d) during the exposure as they continued to stay in contact with the receding edge of the graphite film. Such movements of the nanoparticles may result from the attractive forces by the presence of induced fields from the LSP resonance modes driven by the electron beam. Using the same method as the

aloof beam experiment, the average carbon etching rate for a single nanoparticle is measured to be ≈ 4.31 nm·min^{-1} which is an increase by a factor of ≈ 20 compared to the aloof-beam case (Extended Data Fig. 6). The parallel beam illumination also allows multiple nanoparticles to be illuminated simultaneously (red dotted line, Fig. 3e). As expected, after ≈ 16 min of electron beam illumination, the graphite around multiple nanoparticles also etched away (yellow dashed line, Fig. 3f). By systematically varying the number of simultaneously illuminated nanoparticles (*n*) and the electron flux (*j*), the measured carbon depletion rate from graphite was found to increase linearly with both (Fig. 3g, Extended Data Fig. 7). The latter result is consistent with the observed linear increase in the peak intensity of the LSP resonance at ≈ 6.4 eV with the electron flux (Extended Data Fig. 8). Both the increase in carbon etching with increase LSP peak intensity and its decrease as a function of distance away from the nanoparticle (Fig. 2f) are consistent with the electric field dynamics of LSP resonances in a nanoparticle.

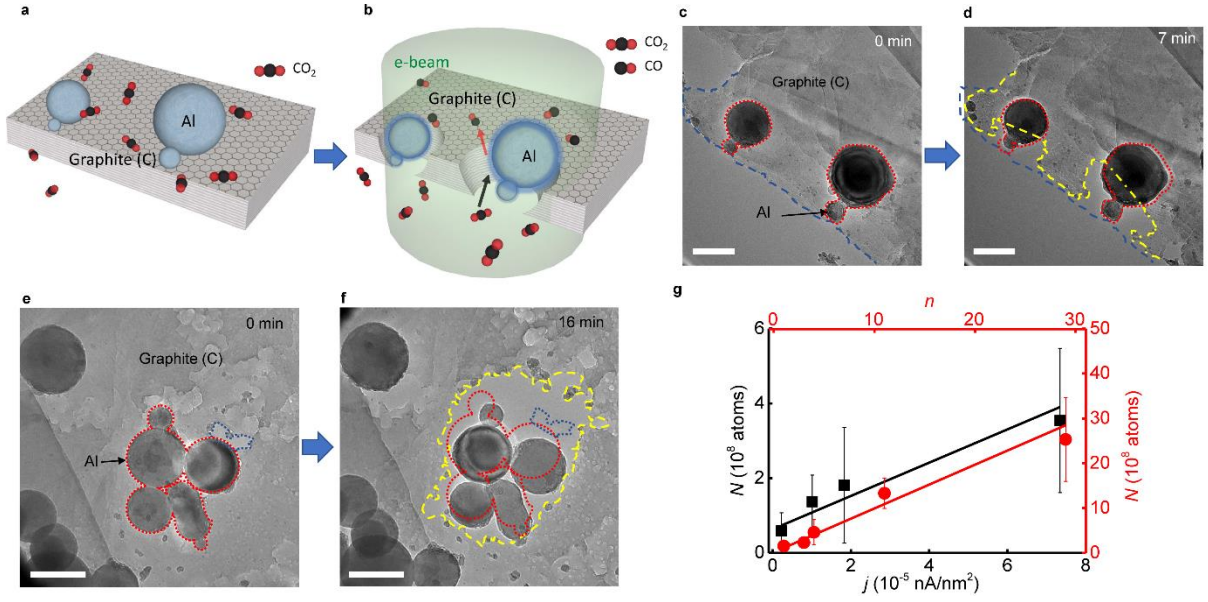

Fig. 3 | Carbon etching as a function of nanoparticle number and electron flux. a-b, A schematic showing the desired configuration of Al nanoparticle on a graphite flake and the expected carbon etching volume (**b**) in a parallel beam configuration. **c-f,** Time-resolved TEM

images showing etching of graphite in CO_2 partial pressure of ≈ 50 Pa with four nanoparticles **c-d**, as well as a cluster of multiple nanoparticles (**e-f**) attached to the graphite, illuminated with an electron flux (j) of ≈ 9.1×10^{-6} nA·nm^{-2}. The blue and yellow dashed, and red dotted lines indicate the outline of the graphite at the beginning and the end of the reaction, and the Al nanoparticles, respectively. **g,** number of carbon atoms (N) etched, obtained from the graphite thickness change (see Supplementary Information) as a function of j for one Al nanoparticle illuminated for ≈ 6 min (black data points), and number of Al nanoparticles (n) illuminated with $j \approx 9.1 \times 10^{-6}$ nA·nm^{-2} for ≈ 6 min (red data points). The black and red lines show the linear fitting of the data. The scale bars are 100 nm. The error represents a single standard deviation of the thickness change statistics surrounding the nanoparticle.

As expected from the dependence of carbon etching on LSP amplitude described above, a spatial variation in carbon etching around the nanoparticles was also observed due to the local field enhancement of coupled LSP resonances (hot spots) between two or more nanoparticles in close proximity to each other. Thickness maps of an area including a three-nanoparticle cluster (Fig. 4a) were acquired before (Fig. 4b) and after electron beam illumination (flux ≈ 9.1×10^{-6} nA·nm^{-2}) for ≈ 15 min in a CO_2 environment at a partial pressure of ≈ 50 Pa (Fig. 4c). The measured thickness variation of carbon etched from the graphite (vertical bars, Fig. 4d) in different regions within the illuminated area clearly shows that the highest carbon etching region is confined to an area close to the interface where the nanoparticles are in contact. Electric field maps for gap modes ranging from 2.3 eV to 7.04 eV (Fig. 4e and Extended Data Fig. 9) were simulated by creating a model for three nanoparticles on graphite (Extended Data Fig. 9a), resembling the experimental images (Fig. 4a). The strongest electric field distribution (Fig. 4e) that approximates the spatial variation in carbon etching (Fig. 4d) is found to maximize at the resonance energy between 6.77 eV and 7.27 eV (Fig. 4f), when monitoring the field amplitude ($\sqrt{E \cdot E^*}$) at the area marked by a blue square in Fig. 4e. We applied a Gaussian fit in Fig. 4f and determine that the strongest field enhancement took place when a gap mode was coupled at 7.04 eV ± 0.01 eV. The gap mode is likely coupled by a roughly parallel field driven by the swift electrons located away from the gap. Although this

is dipolar in nature, our results for one nanoparticle shown in Fig. 1 suggests that coupling to high order modes (such as quadrupole and hexapole) is driven by the aloof electron beam. Additionally, the narrow gap causes the strong plasmon hybridization between the various modes from each of the adjacent nanoparticles, and therefore, allows the parallel field to couple with the nondipolar, high-order modes, such as the hybridized quadrupole and hexapole modes, since they carry a finite dipole moment and become dipole-active[27]. For the three nanoparticles, the plasmon hybridization is expected to redshift the dipole energy of individual nanoparticle (≈ 2.94 eV, Fig. 1b), which may be insufficient to overcome the reported energy barrier for the reverse Boudouard reaction, similar to our control experiment using Au nanoparticles (Extended Data, Fig. 11), where the resonance energies present (approximately 2 eV to 2.4 eV) are lower than the activation energy needed, resulting in no preferential carbon etching near the nanoparticles. These indicate that the field enhancement of high-order mode at about 7.04 eV is viable resulting from the plasmon hybridization at the narrow gap and is essential to provide the activation energy to initiate the endothermic reaction.

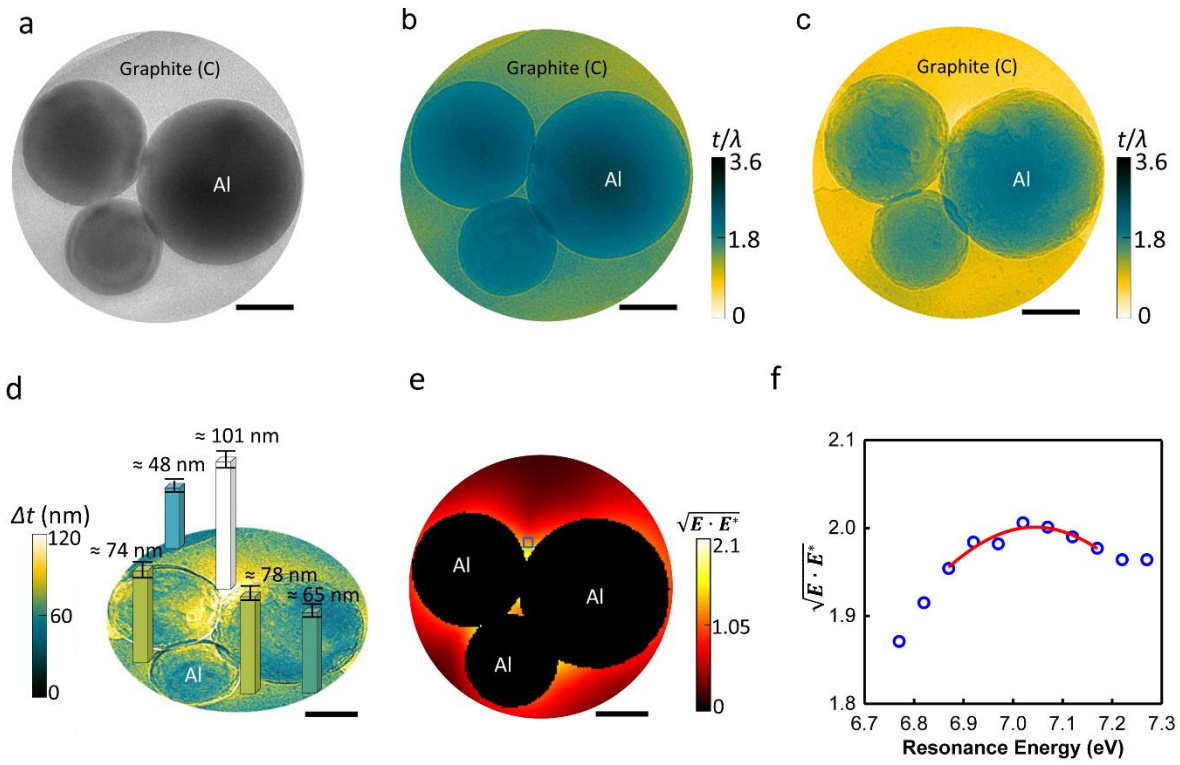

Fig. 4 | Correlation between the reaction rate distribution and the electric field distribution of the LSP resonance. a, TEM image showing three nanoparticles, each in contact with the other two, forming a triangular arrangement. **b-c,** t/λ maps acquired in vacuum before (**b**) and after the reaction (**c**) in vacuum again (post-evacuating CO_2) **d,** Carbon depletion map acquired to quantitatively determine the spatial distribution of carbon etched. The value of each pixel of the map in (d) shows the change of carbon thickness after the electron beam illumination. Four color-coded bars placed at different locations indicate the difference in carbon thickness change. **e,** The simulated electric field distribution of the LSP resonance at 7.04 eV, obtained using the plane-wave excitation without a specific polarization direction that imitates a parallel electron beam illumination. **f,** the electric field enhancement is calculated from the location marked by the blue square in **e** for energies ranging from 6.77 eV to 7.27 eV. The red curve indicates the Gaussian fitting profile used to find the peak center (7.04 eV ± 0.01 eV). The scale bars are 50 nm.

We also performed various control experiments to eliminate any other parameters triggering the etching of graphite at room temperature. Although the absence of appreciable etching away from the nanoparticles in the parallel beam experiments eliminates any significant direct effect of the electron beam, we illuminated graphite with and without the Al nanoparticles, in vacuum, CO_2 and N_2 environment for quantitative comparisons (Extended Data Fig. 10). The measured etching rates

with and without Al nanoparticle in various environments are given in Extended Data Table 1. While uniform etching of the graphite, consistent with radiation damage often reported in TEM experiments[28], was always present (Fig. 5a, Extended Data Table 1), significant preferential etching was not observed after ≈ 6 min of illumination near the Al nanoparticles in vacuum or in N_2, as opposed to in CO_2 (Fig. 5b, Extended Data Fig. 10e), indicating that both Al and CO_2 play an active role in the observed phenomenon.

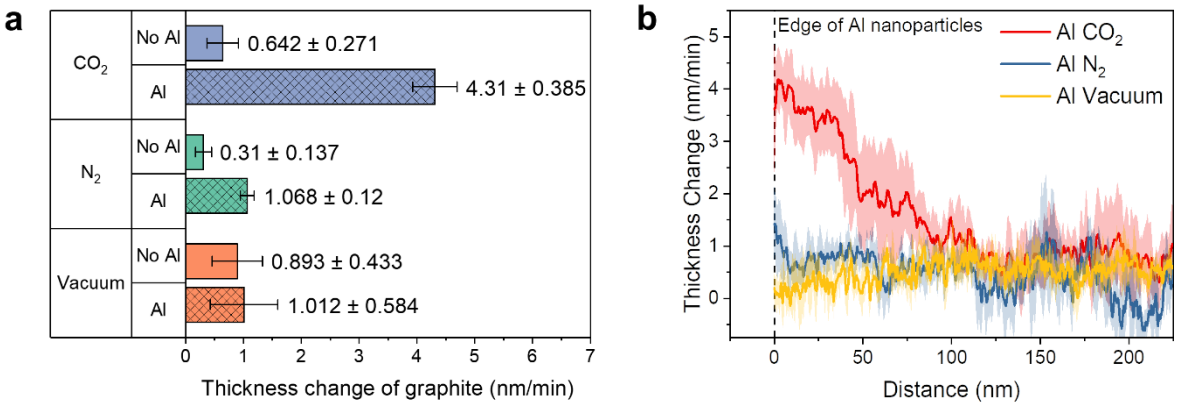

Fig. 5 | Measurement of graphite etching under control experiments. a, comparative graphite etching rate due to electron beam irradiation, with and without Al nanoparticles, in CO_2, N_2 and vacuum. Note that background etching in all conditions except for Al nanoparticles in CO_2 remains around 1 nm·min^{-1}. **b**, graphite thickness change as a function of distance from the surface of the Al nanoparticles in CO_2, N_2 and vacuum indicating the localized increase in graphite etching near the Al nanoparticle in CO_2. The data processing was performed following the same procedure as used for Fig. 2.

Furthermore, we irradiated Au and Al nanoparticles on amorphous carbon, respectively, in a CO_2 environment for the same period of time, and found preferential carbon etching near the Al nanoparticles, but not the Au nanoparticles (Extended Data Fig. 11). We also measured the temperature of the Al nanoparticle, using the bulk plasmon peak position of the Al (see Methods), remained at 25 °C ± 5 °C during the etching process (Extended Data Fig. 12), which is much lower than the reverse Boudouard reaction temperature (> 700 °C)[17]. Finally, core-loss EELS maps show

no carbon signal within the Al nanoparticle after the reaction (Extended Data Fig. 13), confirming that neither CO_2 nor graphite reacted with the Al nanoparticle. We can therefore conclude, within the temporal resolution of our measurement (milliseconds), that a non-thermal process energized by the Al nanoparticles is driving the observed reaction of CO_2 with carbon.

To further confirm the proposed reaction pathway, we used a gas-cell TEM holder (nanoreactor) coupled to a GCMS in the ETEM to analyze the post-reaction gas composition under reaction conditions (see Methods). The peak positioned at ≈ 1.9 min (Fig. 6a), as determined using a 0.05% CO/CO_2 mixture, was assigned to CO and was monitored in the following four nanoreactor environments: pure CO_2 (Fig. 6b, red line), 0.01% CO in CO_2 (Fig. 6b, yellow line), after heating pure graphite at 900 °C in ≈ 10^4 Pa of CO_2 (Fig. 6b, blue line), and finally, after illuminating multiple areas of graphite loaded with Al nanoparticles by an electron flux of 9.1 × 10^{-6} nA·nm^{-2} at room temperature in ≈ 10^4 Pa of CO_2 (Fig. 6b, green line). Measurable CO was detected in the latter three cases, but not in pure CO_2. Detection of CO after heating pure graphite in CO_2 as well as after illuminating Al/graphite sample in CO_2 at room temperature, respectively, confirms that it is a product of the reverse Boudouard reaction in both cases. A semi-quantitative relationship between the amount of carbon etched and the measured CO/CO_2 ratio was found to be linear (Fig. 6c).

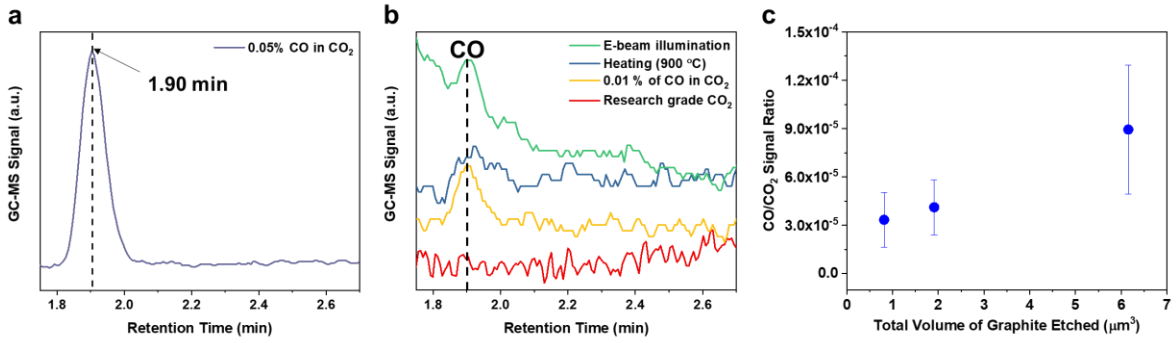

Fig. 6 | Detection of CO as reverse Boudouard reaction product using the GCMS. a, A mixture of 0.05% CO in CO_2 was introduced into the ETEM-GCMS to produce standard MS spectra and the peak observed at ≈ 1.9 min was assigned to CO. **b,** Observed GCMS spectra of CO from pure research grade CO_2 (red), 0.01% CO in CO_2 (yellow), after heating graphite at 900 ˚C in CO_2 (blue), and after electron beam illuminating multiple areas of Al on graphite in CO_2 at room temperature (green). Note that the CO signal is clearly present in the latter three cases except for the research grade CO_2 used in our experiments. Each spectrum was smoothed with a moving average of four data points, normalized by the minimum and stacked for visual clarity. **c,** Relationship between the ratio of CO/CO_2 detected and the measured amount of graphite etched after illuminating 6, 15, and 16 equivalent areas at room temperature (determined by the diameter of the electron beam) for 30 min each with the electron beam.

In conclusion, we show that the reverse Boudouard reaction ($CO_{2(g)} + C_{(s)} \rightarrow 2CO_{(g)}$) can be initiated by high-energy LSP resonances of Al nanoparticles at room temperature. In our approach, an electron beam is used as a broadband "light source" to excite various LSP resonances of Al nanoparticles to drive the reaction. The amount of CO produced in our experiments is small (≈ ppm level) due to the small reaction volume (≈ 10^8 nm^3) and is therefore outside the range of the GCMS calibration curve so clear quantification could not be made. Instead, the measured carbon thickness change is used to quantify the conversion of reactant to product near the nanoparticle surface. Furthermore, a correlation between the local field enhancement of coupled LSP resonances (with an energy of ≈ 7 eV) and the highest amount of carbon etched for the three-nanoparticle cluster indicates that high-energy plasmons are responsible for driving the reaction. As the most earth-abundant metal, the use of Al promises a novel path for CO_2 reduction by any form of carbon. Our approach also showcases electron-excited LSP resonances in an ESTEM provide a direct observation and quantification method to initiate and probe chemical reactions at the nanoscale and opens a pathway towards investigating other similar reactions *in situ*, with unprecedented detail.

Data availability

The data that support the findings of this study are available from the corresponding author upon reasonable request.

Acknowledgments

We gratefully thank Devika Sil (NIST, now at IBM) for useful discussions. C.W., W.D.Y., A.B. and A.A. acknowledge support under the Cooperative Research Agreement between the University of Maryland and the National Institute of Standards and Technology Physical Measurement Laboratory, Award 70NANB14H209, through the University of Maryland.

Author contributions

C.W., W.D.Y., and R.S. conceived and designed the research; C.W. prepared the samples, conducted *in situ* measurements in the ESTEM and processed the data. W.D.Y. and A.B. carried out electromagnetic BEM calculations; A. A. contributed to designing the models for simulation; D. R. and A. A. contributed to the design of the experiments and the analysis of the results. R. M. and D.R. designed and helped in conducting the GCMS experiments. All authors contributed to writing the manuscript.

Competing interests

The authors declare no competing interests.

Methods

Preparation of Al covered graphite on lacey carbon TEM grids

Graphite (99.99% purity) and Al nanoparticle (99.7% purity) suspensions are prepared separately by dispersion in ethanol followed by ≈ 20 min of sonication. Graphite was chosen as the carbon source because its thickness change can be quantified in terms of number of carbon atoms consumed during the reaction, *i.e.*, a measure of the reaction rate (see Supplementary Information). To prepare the Al covered graphitic TEM grids, first the graphite suspension is drop cast onto a lacey carbon TEM grid, followed by ≈ 10 min of heating under an infrared lamp to dry out the residual ethanol. The Al nanoparticle suspension is then drop cast onto the dried lacey carbon grid with the graphite deposit, followed by ≈ 10 min of heating under the infrared lamp to dry out the residual ethanol.

Simulations of LSP modes excited by electron beam

LSP modes of Al nanoparticle excited by an electron beam are simulated using the metallic nanoparticle boundary element method (MNPBEM) toolbox[29]. The boundary element method (BEM) approach is designed to solve Maxwell's equations in a dielectric environment where materials with homogeneous and isotropic dielectric functions are divided by discretized interfaces. In this work, we use this approach to simulate: (*i*) the electron energy-loss probability and (*ii*) the electric field distribution near the Al nanoparticle surface. The simulated electric field distribution at resonance represents the enhancement of electric field amplitude resulting from the LSPs excited by either a static electron beam outside one Al nanoparticle (aloof electron beam) or a parallel electron beam illuminating multiple Al nanoparticles simultaneously. The plane-wave excitation without a specific polarization direction is only used for the simulations that imitate a parallel electron beam.

Environmental scanning transmission electron microscope (ESTEM) measurements

Al nanoparticles covered graphitic flakes on the lacey carbon TEM grid is transferred to the ESTEM, operated at 80 kV. CO_2 and N_2 gas (research grade: 99.999% purity) under controlled pressures were introduced in the sample area using mass flow controllers[30]. A monochromated electron beam, with energy resolution of ≈ 0.08 eV, is used to excite LSP modes, and to collect images and EELS data. During EELS acquisition, a convergence semi-angle of ≈ 7.8 mrad and the collection semi-angle of ≈ 15.2 mrad is used. EELS spectrum images, three-dimensional (3D) data cubes that contain energy-loss information in the *z*-direction at each pixel of a STEM-ADF image, were acquired by scanning the electron beam across a region of interest while recording a spectrum for each pixel. The thickness maps (see Supplementary Information) were acquired in vacuum (≈ 10^{-5} Pa), before introducing CO_2 and after reaction period followed by evacuation of the sample area back to vacuum, using either energy filtered TEM, or EELS spectrum images acquired in STEM mode. The carbon depletion amounts, in terms of thickness change, are obtained by subtracting the value of each pixel of the thickness map acquired after the reaction from the one acquired before the reaction. Before subtraction, the two thickness maps are aligned using an image cross-correlation based algorithm to determine and remove the relative offset between them. The temperature of the Al nanoparticles is measured using the Al bulk plasmon peak acquired using EELS[31].

Drift corrected aloof excitation of localized surface plasmon resonance

To excite the localized surface plasmon resonance of Al nanoparticle without exciting bulk plasmon or other ionizing events in Al or graphite, the electron beam is placed at an aloof position near an Al nanoparticle that is partially attached to the graphite flake. Drift correction is applied to

maintain the beam position with respect to the graphite flake during the long illumination time. The area used in drift correction as a reference is chosen such that it's further away from the Al nanoparticle of interest, and that the path between the reference area and the aloof potion does not overlap with the Al nanoparticle of interest. Care was taken to make sure the allowed drift of the beam position is less than the distance between the aloof position and the Al nanoparticle surface (≈ 6 nm). The drift interval was chosen such that between two corrections the specimen drifts less than 0.5 nm.

Detection of the reaction product:

A MEMS Nano-Reactor inside an in situ TEM holder was used as a sample carrier in the ETEM. The holder was coupled to a home build gas supply system and to a gas chromatograph-mass spectrometer (GCMS) that was used to detect CO in the post-reaction exhaust. First, we identified the peak position of the instrument using 0.05% CO in CO_2 flowing through the gas-cell which gave us a peak at ≈ 1.9 min for CO. To ensure our research grade CO_2 did not provide a false positive, we measured pure CO_2 which did not give a measurable CO peak. We then incrementally reduced the CO concentration in the mixture gas of CO and CO_2 to establish a standard CO calibration curve. Our limit of detection was determined to be approximately 100 ppm (0.01 %) CO in CO_2. Finally, we performed two types of reverse Boudouard reaction based experiments. Prior to any measurements, pure CO_2 was purged through the lines including the nanoreactor. Negative controls were obtained to ensure the system was clear of any gases from previous measurements. Then, for the first experiment, the nanoreactor was loaded with graphite only, inserted in the ETEM column and filled with ≈ 10^4 Pa of CO_2. The sample was heated to 900 ˚C without illumination in static mode (outlet valve closed). After 3 hours, the reactor valve to the

GCMS sample loop was opened and an injection was made to detect gas products. The presence of CO strongly supports that, as expected, the reverse Boudouard reaction had taken place. Next, we loaded another chip containing both Al nanoparticles and carbon in the nanoreactor and filled the same amount of CO_2 ($\approx 10^4$ Pa). This time we illuminated multiple areas (each with the size of $\approx 1.5 \times 10^6$ nm^2) of the sample with an electron flux of $\approx 9.1 \times 10^{-6}$ nA·nm^{-2} for 30 min each, without heating. We once again opened the valve to the GCMS after illuminating 24 areas and the effluent gas was found to contain CO on the order to 100 ppm, but outside the range of the calibration curve so clear quantification could not be made. The amount of carbon etched, and CO produced was also measured after illuminating 6, 15 and 16 equivalent areas under identical illumination conditions for 30 minutes each.

References

1 Zhang, Y. *et al.* Surface-plasmon-driven hot electron photochemistry. *Chemical reviews* **118**, 2927-2954 (2017).

2 Christopher, P., Xin, H. & Linic, S. Visible-light-enhanced catalytic oxidation reactions on plasmonic silver nanostructures. *Nature Chemistry* **3**, 467 (2011).

3 Mukherjee, S. *et al.* Hot electrons do the impossible: plasmon-induced dissociation of H2 on Au. *Nano Letters* **13**, 240-247 (2012).

4 Zhou, L. *et al.* Aluminum Nanocrystal as a Plasmonic Photocatalyst for Hydrogen Dissociation. *Nano Letters* (2016).

5 Hartland, G. V., Besteiro, L., Johns, P. & Govorov, A. O. What's so Hot about Electrons in Metal Nanoparticles? *ACS Energy Letters* (2017).

6 Christopher, P., Xin, H., Marimuthu, A. & Linic, S. Singular characteristics and unique chemical bond activation mechanisms of photocatalytic reactions on plasmonic nanostructures. *Nature Materials* **11**, 1044 (2012).

7 Yang, J., Guo, Y., Lu, W., Jiang, R. & Wang, J. Emerging Applications of Plasmons in Driving CO2 Reduction and N2 Fixation. *Advanced Materials* **30**, 1802227 (2018).

8 Wang, P. *et al.* Ag@ AgCl: a highly efficient and stable photocatalyst active under visible light. *Angewandte Chemie International Edition* **47**, 7931-7933 (2008).

9 Christopher, P., Ingram, D. B. & Linic, S. Enhancing photochemical activity of semiconductor nanoparticles with optically active Ag nanostructures: photochemistry mediated by Ag surface plasmons. *The Journal of Physical Chemistry C* **114**, 9173-9177 (2010).

10 Ingram, D. B. & Linic, S. Water splitting on composite plasmonic-metal/semiconductor photoelectrodes: evidence for selective plasmon-induced formation of charge carriers near the semiconductor surface. *Journal of the American Chemical Society* **133**, 5202-5205 (2011).

11 Zheng, Z. *et al.* Facile in situ synthesis of visible-light plasmonic photocatalysts M@ TiO 2 (M= Au, Pt, Ag) and evaluation of their photocatalytic oxidation of benzene to phenol. *Journal of Materials Chemistry* **21**, 9079-9087 (2011).
12 Mubeen, S. *et al.* An autonomous photosynthetic device in which all charge carriers derive from surface plasmons. *Nature Nanotechnology* **8**, 247 (2013).
13 Zhou, L. *et al.* Quantifying hot carrier and thermal contributions in plasmonic photocatalysis. *Science* **362**, 69-72 (2018).
14 Kale, M. J., Avanesian, T. & Christopher, P. Direct photocatalysis by plasmonic nanostructures. *ACS Catalysis* **4**, 116-128 (2013).
15 Zhang, X., Chen, Y. L., Liu, R.-S. & Tsai, D. P. Plasmonic photocatalysis. *Reports on Progress in Physics* **76**, 046401 (2013).
16 Yang, W.-C. D. *et al.* Site-selective CO disproportionation mediated by localized surface plasmon resonance excited by electron beam. *Nature Materials* **18**, 614 (2019).
17 Hunt, J. *et al.* Microwave-specific enhancement of the carbon–carbon dioxide (Boudouard) reaction. *The Journal of Physical Chemistry C* **117**, 26871-26880 (2013).
18 Marchon, B., Tysoe, W., Carrazza, J., Heinemann, H. & Somorjai, G. Reactive and kinetic properties of carbon monoxide and carbon dioxide on a graphite surface. *The Journal of Physical Chemistry* **92**, 5744-5749 (1988).
19 Strange, J. & Walker Jr, P. Carbon-carbon dioxide reaction: Langmuir-Hinshelwood kinetics at intermediate pressures. *Carbon* **14**, 345-350 (1976).
20 Batson, P. A new surface plasmon resonance in clusters of small aluminum spheres. *Ultramicroscopy* **9**, 277-282 (1982).
21 McClain, M. J. *et al.* Aluminum nanocrystals. *Nano Letters* **15**, 2751-2755 (2015).
22 Fujimoto, F. & Komaki, K. I. Plasma Oscillations Excited by a Fast Electron in Metallic Particle. *J Phys Soc Jpn* **25**, 1679-1687, doi:Doi 10.1143/Jpsj.25.1679 (1968).
23 Hohenester, U. Simulating electron energy loss spectroscopy with the MNPBEM toolbox. *Computer Physics Communications* **185**, 1177-1187, doi:10.1016/j.cpc.2013.12.010 (2014).
24 Hohenester, U., Ditlbacher, H. & Krenn, J. R. Electron-energy-loss spectra of plasmonic nanoparticles. *Physical Review Letters* **103**, 106801 (2009).
25 Busch, K., König, M. & Niegemann, J. Discontinuous Galerkin methods in nanophotonics. *Laser & Photonics Reviews* **5**, 773-809, doi:10.1002/lpor.201000045 (2011).
26 Seemala, B. *et al.* Plasmon-mediated Catalytic O2 Dissociation on Ag Nanostructures: Hot Electrons or Near Fields? *ACS Energy Letters* **4**, 1803-1809 (2019).
27 Nordlander, P., Oubre, C., Prodan, E., Li, K. & Stockman, M. I. Plasmon Hybridization in Nanoparticle Dimers. *Nano Letters* **4**, 899-903, doi:10.1021/nl049681c (2004).
28 Egerton, R. F., Li, P. & Malac, M. Radiation damage in the TEM and SEM. *Micron* **35**, 399-409, doi:10.1016/j.micron.2004.02.003 (2004).
29 Hohenester, U. & Trügler, A. MNPBEM–A Matlab toolbox for the simulation of plasmonic nanoparticles. *Computer Physics Communications* **183**, 370-381 (2012).
30 Sharma, R. An environmental transmission electron microscope for in situ synthesis and characterization of nanomaterials. *Journal of Materials Research* **20**, 1695-1707 (2005).
31 Mecklenburg, M. *et al.* Nanoscale temperature mapping in operating microelectronic devices. *Science* **347**, 629-632 (2015).

Supplementary Information

Endothermic Reaction at Room Temperature enabled by Deep-Ultraviolet Plasmons

Canhui Wang[1,2], Wei-Chang D. Yang[1,2#], David Raciti[3], Alina Bruma[1,2], Ronald Marx[4], Amit Agrawal[1,2], and Renu Sharma[1*]

1. Physical Measurement Laboratory, National Institute of Standards and Technology, Gaithersburg, MD 20899, USA.

2. Institute for Research in Electronics and Applied Physics & Maryland NanoCenter, University of Maryland, College Park, MD 20742, USA.

3. Measurement and Materials Laboratory, National Institute of Standards and Technology, Gaithersburg, MD 20899, USA.

4. DENSsolutions B.V., Delft 2628 ZD, The Netherlands.

* Correspondence to: renu.sharma@nist.gov

Secondary Corresponding Author: david.yang@nist.gov

Morphology, elemental distribution and EELS map

Extended Data Fig. 1a shows an annual dark field (ADF) image of a typical Al nanoparticle attached to the graphite flake. Electron energy-loss spectra (EELS) extracted from the spectrum image acquired from an area containing an Al nanoparticle (green dashed box, Extended Data Fig. 1a) indicates the presence of aluminum (Al), oxygen (O), and carbon (C) (Extended Data Fig. 1b). Elemental maps for aluminum metal (Al^0) (Extended Data Fig. 1c), O (Extended Data Fig. 1d), and carbon C (Extended Data Fig. 1e), obtained from the core-loss EELS spectrum image show an Al/Al_2O_3 core-shell structure (Extended Data Fig. 1f), with the shell being ≈ 4 nm thick Al_2O_3

(yellow), and the core being Al^0 (magenta). Carbon (blue) is confined to the graphite flake. This information was used to construct a model (Fig. 1c) to represents the Al nanoparticle attached to the graphite flake for electron energy loss probability and electric field distribution simulation using metal nanoparticle boundary element (MNPBEM) toolbox[32].

Preferential carbon etching around Al nanoparticle and field decay

A plasmonic field decays exponentially away from the nanoparticle surface, with a 1/*e* decay length in the surrounding dielectric environment given by[33]:

$$z_d = \frac{\lambda_0}{2\pi}\sqrt{\left|\frac{\epsilon_m' + \epsilon_d}{\epsilon_d^2}\right|}$$

where ϵ_m' is the real part of the dielectric permittivity of metal, and ϵ_d is the permittivity of dielectric medium surrounding the metal. For free-space (ϵ_d = 1), the calculated values for the plasmon decay length of the dipole, quadrupole and the hexapole modes for Al using both the Palik[34] and the CRC[35] permittivity database are calculated to be:

	3.9 eV (317 nm)	**5.8 eV (215 nm)**	**7 eV (177 nm)**
Al – Palik	186 nm	79 nm	47 nm
Al – CRC	186 nm	79 nm	48 nm

In the presence of graphite, the corresponding decay length of the fields associated with these three modes using a wavelength dependent dielectric function[36] are given by:

	3.9 eV (317 nm)	**5.8 eV (215 nm)**	**7 eV (177 nm)**
Al – Palik Graphite[36]	79 nm	29 nm	12 nm

These values provide a first order estimate of the spatial extent over which plasmon fields are present around the nanoparticle in point-contact with a graphite support. These values are also consistent with the mode calculations performed using the DGTD technique (see Extended Data Fig. 5) and the MNPBEM simulations (Fig. 1), and clearly illustrate that there are optical fields present at distances larger than a few 10's of nm away from the nanoparticle surface.

Quantification of carbon etching

The intensities in the EELS spectrum were used to obtain the thickness of the specimen, t, using the log-ratio method[37]:

$$t = \lambda \ln\left(\frac{I_t}{I_0}\right)$$

where, λ is the mean free path (MFP), defined as the average distance traveled by a moving electron between successive collisions in the specimen, I_t is total transmitted electrons, I_0 represents inelastically scattered electrons. The value of λ depends on the energy of incident electrons, scattering and collection angles for the spectrum, and the nature of the sample. We collected images using a 14-eV slit around the zero-loss peak (I_0) and without a slit using all electrons (I_t). A t/λ map was then obtained using a log-ratio of the two images acquired based on the above equation. The value of λ for graphite under our experimental condition was calculated to be $\approx$ 109.91 nm[38] and was used to obtain the value of t in nm.

The etching rate of carbon was determined by measuring the carbon thickness change using EFTEM or STEM-EELS data. A t/λ map is first acquired in vacuum (Extended Data Fig. 6a). After the reaction in CO_2, the sample chamber was evacuated (to avoid the contribution of CO_2

gas to the thickness measurement) before acquiring the second t/λ map (Extended Data Fig. 6b). A thickness change map (carbon depletion map) can then be acquired by subtracting the t/λ map acquired after the reaction from the one acquired before the reaction (Extended Data Fig. 6c). Cross-correlation was applied to align the before and after reaction maps to correct for possible drift of the specimen between the data acquisition of the two maps.

The measured decrease in graphite thickness was then converted to the number of carbon atoms used in the reaction by calculating the volume of the carbon etched as follows:

$$\mathrm{V} = t' \bullet a$$

where V is the volume, t' is average thickness difference obtained from the thickness maps (described above) and *a* is the selected area that included the etched region. The number of carbon atoms etched either in terms of mass or number of molecules can then be obtained by taking the density of graphite into consideration, using the following equations:

$$m = \rho_g \cdot V$$

$$n = \frac{N_A \cdot m}{A_{r,std}}$$

where m is the amount of carbon etched in terms of mass, ρ_g is the density of graphite, n is the number of carbon atoms, N_A is the Avogadro constant, and $A_{r,std}$ is the standard atomic weight.

Quantification of graphite etching with and without Al nanoparticle in vacuum, N_2 and CO_2: As negligible etching of graphite was observed away from the Al nanoparticles during all experiments performed and reported here, the ionization effect of high energy electrons cannot be ruled out. Therefore, graphite samples with and without the Al nanoparticle were illuminated by the same electron flux in vacuum (Extended Data Fig. 10, a-b), N_2 (Extended Data Fig. 10, c-d)

and CO_2 (Extended Data Fig. 10, e-f), for comparison. Significant preferential etching was not observed after ≈ 6 min of illumination near the Al nanoparticles in vacuum or in N_2, as opposed to in CO_2 (Fig. 3, Fig. 5, Extended Data Fig. 10e,), indicating that both Al and CO_2 play an active role in the observed phenomenon. The etching of carbon further away from the Al nanoparticle is comparable to the etching when Al is not present or with the Al nanoparticle in vacuum or N_2 environment (Fig. 5b), and therefore can be attributed to the ionization effect of the electron beam. The total etching rate in CO_2 environment is ≈ 7 times higher when the Al nanoparticle is present (Fig. 5a, Table 1). After factoring in the carbon etching due to ionization, we attribute the higher etching rate near the Al nanoparticles to the reverse Boudouard reaction initiated by the LSP resonance of the Al nanoparticles. Therefore, the amount of carbon etching due to the reverse Boudouard reaction can be measured by selecting only the area near the Al nanoparticle, with an additional step of subtracting the amount of carbon etching contributed by ionization.

LSP resonance energy versus reaction activation energy

Aluminum nanoparticles are chosen for the proposed reaction pathway because they support localized plasmon modes at energies greater than the reaction barrier. To prove this hypothesis, we performed a negative control experiment with Au nanoparticles of diameter ≈ 50 nm. The dominant plasmon mode supported by the Au nanoparticle is at an energy of ≈ 2.3 eV which is not sufficient to trigger the reverse Boudouard reaction. Indeed, whereas uniform etching of amorphous carbon due to radiation damage is present, no preferential etching around the Au nanoparticles is observed (Extended Data Fig. 11). Furthermore, as additional evidence of this mechanism, the observed preferential etching near the Al nanoparticle only occurs in the presence of CO_2, but not in other gases.

Temperature measurement during the reverse Boudouard reaction:

The position of plasmon the peak in the EEL spectrum has been shown to be sensitive to the temperature of the nanoparticle[31]. First, we verified the robustness of this temperature measurement technique by intentionally heating the system while measuring the plasmon peak position shift (Extended Data Fig. 12a) with temperature. We then acquired the bulk plasmon peak of the Al nanoparticle in vacuum and in CO_2 (Extended Data Fig. 12b). The temperature calculated based on the Al bulk plasmon peak position indicates that the temperature of the nanoparticle remained within the measurement error of ± 5 °C during the reaction[7]. It has also been estimated that the electron beam induced temperature increase in the case of carbon film is less than 1.5 °C under the illumination electron flux used in our experiments[8].

Chemical composition of the sample before and after the reaction

EELS maps of an Al nanoparticle on graphite in the vacuum, in CO_2, and after evacuating CO_2 are acquired. Elemental maps of the Al nanoparticle can then be extracted from these EELS maps and show the elemental distribution of the nanoparticle before (Extended Data Fig. 13a), and after (Extended Data Fig. 13b) the reverse Boudouard reaction. The comparison of the elemental maps shows that after the carbon etching, there is not a measurable amount of carbon present in the nanoparticle, i.e. carbon is not reacting with the Al oxide shell or the Al core.

References

32 Hohenester, U. & Trügler, A. MNPBEM–A Matlab toolbox for the simulation of plasmonic nanoparticles. *Computer Physics Communications* **183**, 370-381 (2012).

33 Novotny, L. & Hecht, B. in *Principles of Nano-Optics* Ch. 12, 369-413 (2012).

34 Palik, E. D. *Handbook of Optical Constants of Solids* (Elsevier Inc.,, 1997).

35 Shiles, E., Sasak T. , iInokuti, M. ,, Smith., D.Y. . Self-consistency and sum-rule tests in the Kramers-Kronig analysis of optical data: Applications to aluminum. *Physical Review B* **22**, 1612 (1980).

36 Djurišić, A. B. & Li, E. H. Optical properties of graphite. *Journal of Applied Physics* **85**, 7404-7410, doi:10.1063/1.369370 (1999).
37 Egerton, R. F. *Electron energy-loss spectroscopy in the electron microscope*. (Springer, 2011).
38 Tanuma, S., Powell, C. J. & Penn, D. R. Calculations of electron inelastic mean free paths (IMFPS). IV. Evaluation of calculated IMFPs and of the predictive IMFP formula TPP-2 for electron energies between 50 and 2000 eV. *Surface and interface analysis* **20**, 77-89 (1993).

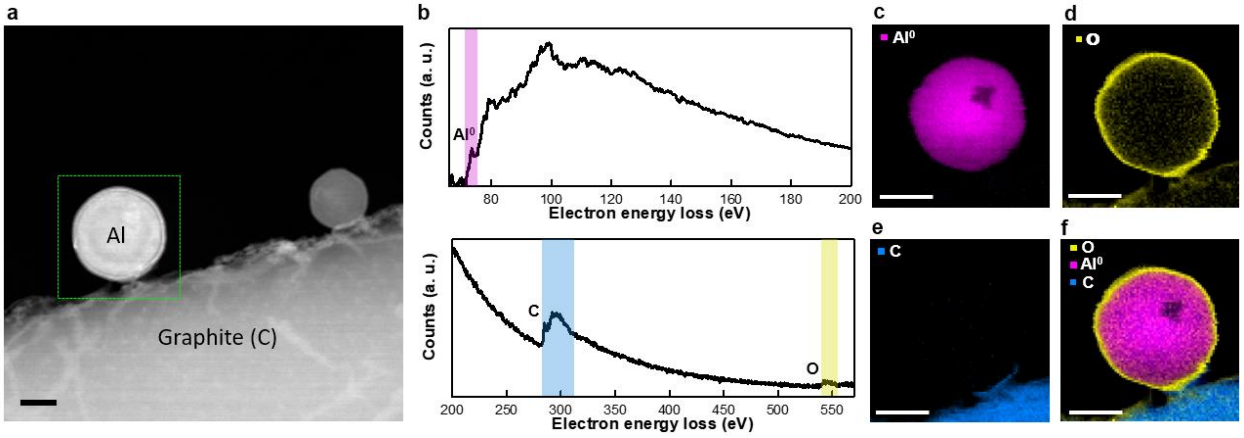

Extended Data Fig. 1 | Electron microscopy characterization of the morphology and the elemental distribution of an Al nanoparticle. a, ADF image of two Al nanoparticles attached to a graphite flake. The green dashed box shows the area used to acquire the EELS spectrum images. **b,** EELS spectra extracted from the spectrum image acquired. The highlighted magenta, blue and yellow regions mark the Al L-edge, C K-edge and O K-edge, used to extract the elemental maps, respectively. **c**-**e,** Elemental maps extracted from the spectrum image acquired for (**c**) aluminum metal (magenta, Al^0), (**d**) oxygen (yellow, O), and (**e**) carbon (blue, C). **f**, Composite map of O, Al^0 and C. The elemental maps show an Al/Al_2O_3 core-shell structure, with the core being Al metal, and the shell being a thin layer of Al_2O_3. The scale bars are 50 nm.

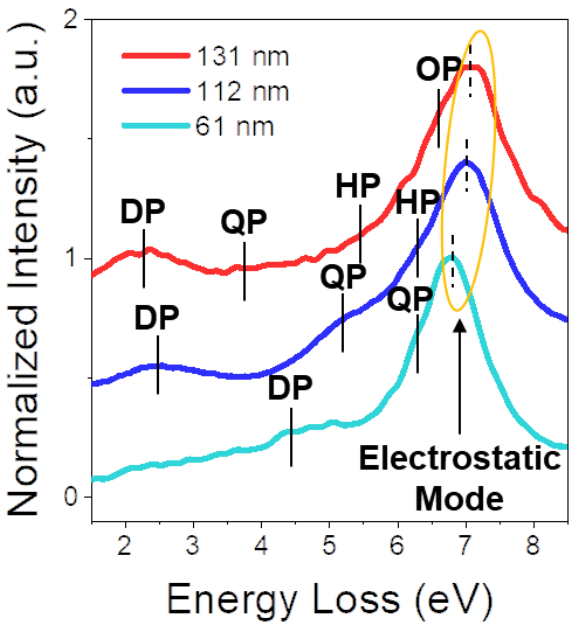

Extended Data Fig. 2 | Nanoparticle size effect on electron beam excited LSP resonance modes. Measured EELS for nanoparticles of different diameters: 61 nm (turquoise), 112 nm (blue), 131 nm (red), with a uniform Al_2O_3 shell of ≈ 4 nm, which form an antenna configuration on graphite. The aloof electron beam for the EELS measurements was located at the far side of the nanoparticles away from the graphite, equivalently illustrated in Fig. 1a. The simulated LSP resonance mode energies of dipole (DP), quadrupole (QP), and hexapole (HP) are indicated by the black, solid markers, respectively. The simulated locations of the electrostatic plasmon mode are indicated by the black, dashed lines. The intensity has been normalized to the strongest peak of each spectrum for the ease of comparison.

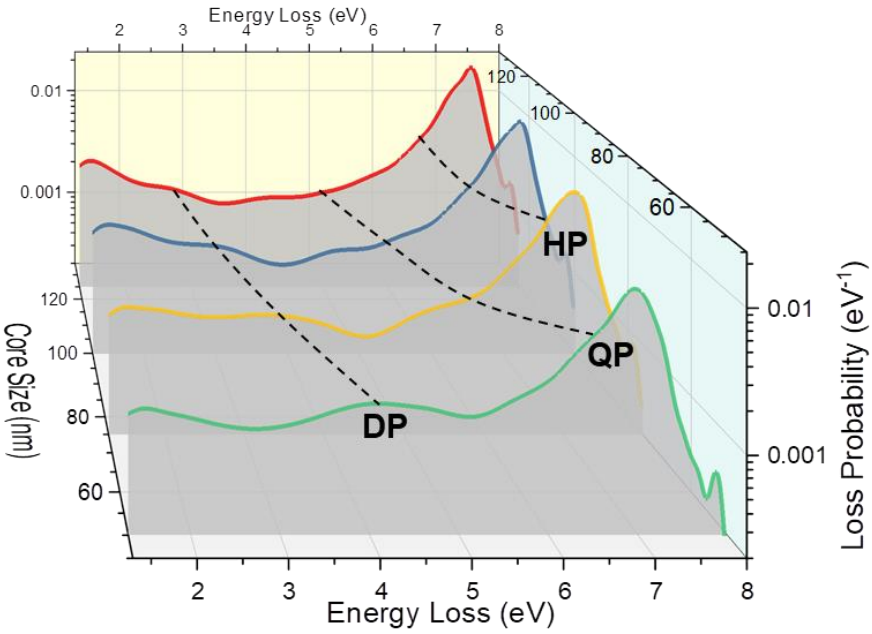

Extended Data Fig. 3 | Numerical calculation of electron beam excited LSP resonance modes. Simulated electron energy-loss probability for Al/Al_2O_3 nanoparticles of different Al core diameters: 45 nm, 75 nm, 100 nm, and 125 nm, with a uniform Al_2O_3 shell of 4.3 nm, using MNPBEM. In the 3D meshed model, the nanoparticle forms an antenna configuration with the graphite. The aloof electron beam is located at the far side of the nanoparticle away from the graphite. The LSP resonance mode energies of dipole, quadrupole, and hexapole are indicated by the dashed lines.

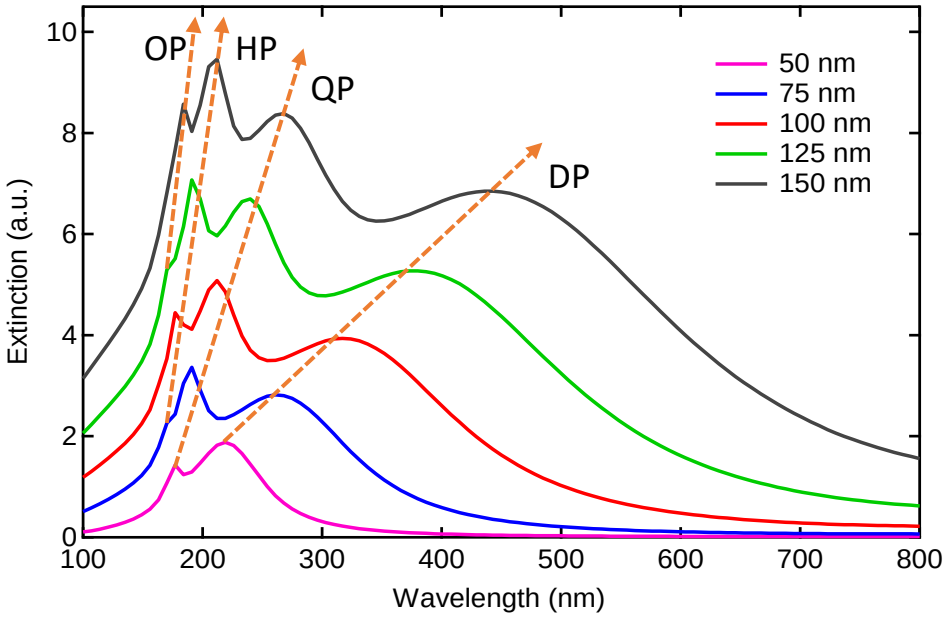

Extended Data Fig. 4 | Numerical calculation of optically excited LSP resonance mode. Extinction spectra for Al nanoparticles of diameters ranging from 50 nm to 150 nm calculated

using the Mie scattering theory. The Al nanoparticles are coated with a 4 nm thick shell of Al_2O_3. DP, QP, HP and QP in the plots correspond respectively to the dipole, quadrupole, hexapole and octupole modes supported by the nanoparticle.

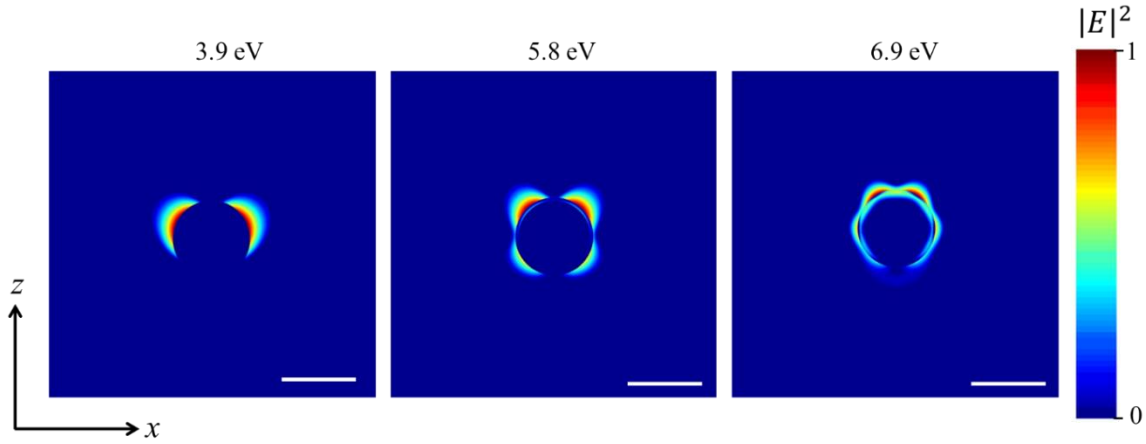

Extended Data Fig. 5 | Numerical calculation of electric field distributions for Al nanoparticles. Electric field intensity distribution calculated using a full three-dimensional electromagnetic Maxwell's equation solver based on the DGTD technique. The three panels correspond to the intensity distribution for the dipole, quadrupole and hexapole modes of a 100 nm Al nanoparticle. The scale bars are 100 nm.

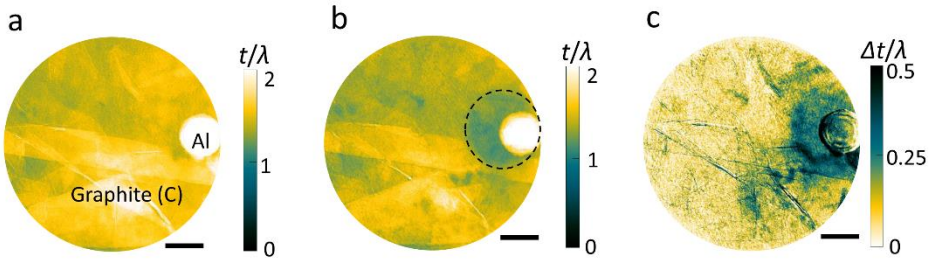

Extended Data Fig. 6 | Measurement of carbon etching using EFTEM during the reaction. a, Thickness (t/λ) map of an Al nanoparticle on graphite acquired in vacuum. **b,** t/λ map of the same area acquired in vacuum after ≈ 6 min of electron beam excitation ($j \approx 9.1 \times 10^{-6}$ nA·nm^{-2}) in CO_2 with a partial pressure of 50 Pa. After the reaction in CO_2, the gas was evacuated before acquiring the second t/λ map to avoid the contribution of the gas to the thickness measurement. Note that the graphite thickness dropped from ≈ 1.5 λ in **a** to ≈ 1.2 λ in the area around Al nanoparticle. **c,** Carbon depletion map, acquired by subtracting the value of each pixel in **b** from **a**. The micrographs are masked based on the circular shape of the electron beam. The scale bars are 200 nm.

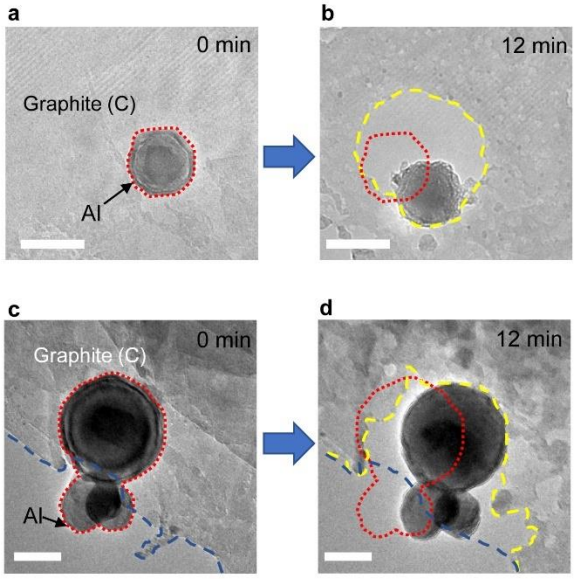

Extended Data Fig. 7 | Etching of carbon as the number of nanoparticle increases. a-d, Time-resolved TEM images showing etching of graphite in ≈ 50 Pa CO_2 environment with one nanoparticle (**a-b**), and three nanoparticles (**c-d**), attached to the graphite, illuminated with an electron flux of ≈ 9.1×10^{-6} nA·nm^{-2} for a duration of ≈ 12 min. The red dotted, blue and yellow dashed lines indicate the outline of Al nanoparticles and the graphite at the beginning and the end of the reaction respectively. The etched area increases with nanoparticle number. The scale bars are 50 nm.

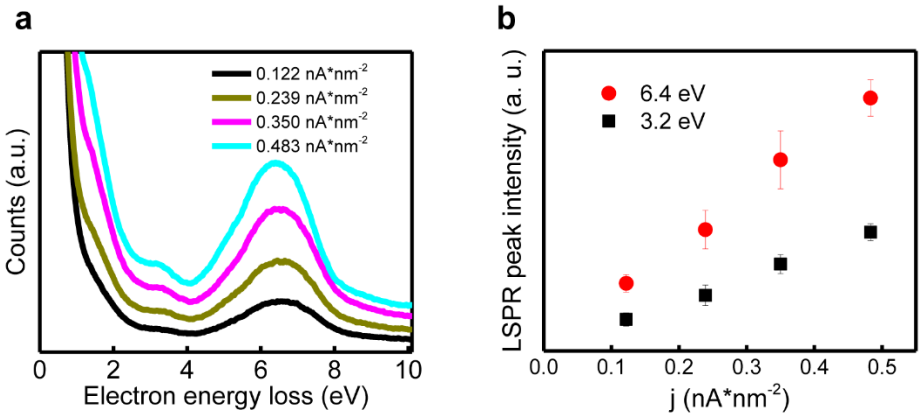

Extended Data Fig. 8 | a, EELS spectra showing excitation of LSP resonance under varying electron beam flux. **b,** The linear relationship between the electron beam flux and the intensity of the peaks at ≈ 6.4 eV and ≈ 3.2 eV. Error bar is one standard deviation from fitting the peaks to a Gaussian function.

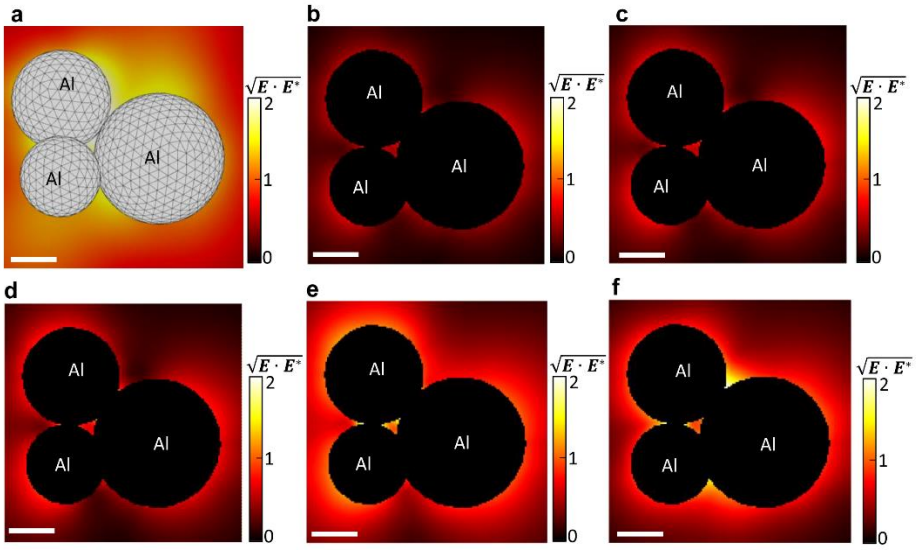

Extended Data Fig. 9 | Simulated electric field distribution maps of the three-nanoparticle cluster. a, Simulated electric field distribution map around a three-particle cluster at 7.04 eV obtained using the MNPBEM simulations (*23*), in the early stage of carbon etching, assuming the graphite is tangent to the two large Al nanoparticles. Although the field amplitude under the Al nanoparticle cannot be seen in the projected view, the field enhancement between the two nanoparticles is visible. **b-f,** The electric field at 2.3 eV (**b**), 3.3 eV (**c**), 4.3 eV (**d**), 5.3 eV (**e**), 6.3 eV (**f**), is distributed on the graphite as the areas of graphite under the Al nanoparticle are etched away. The scale bars are 50 nm.

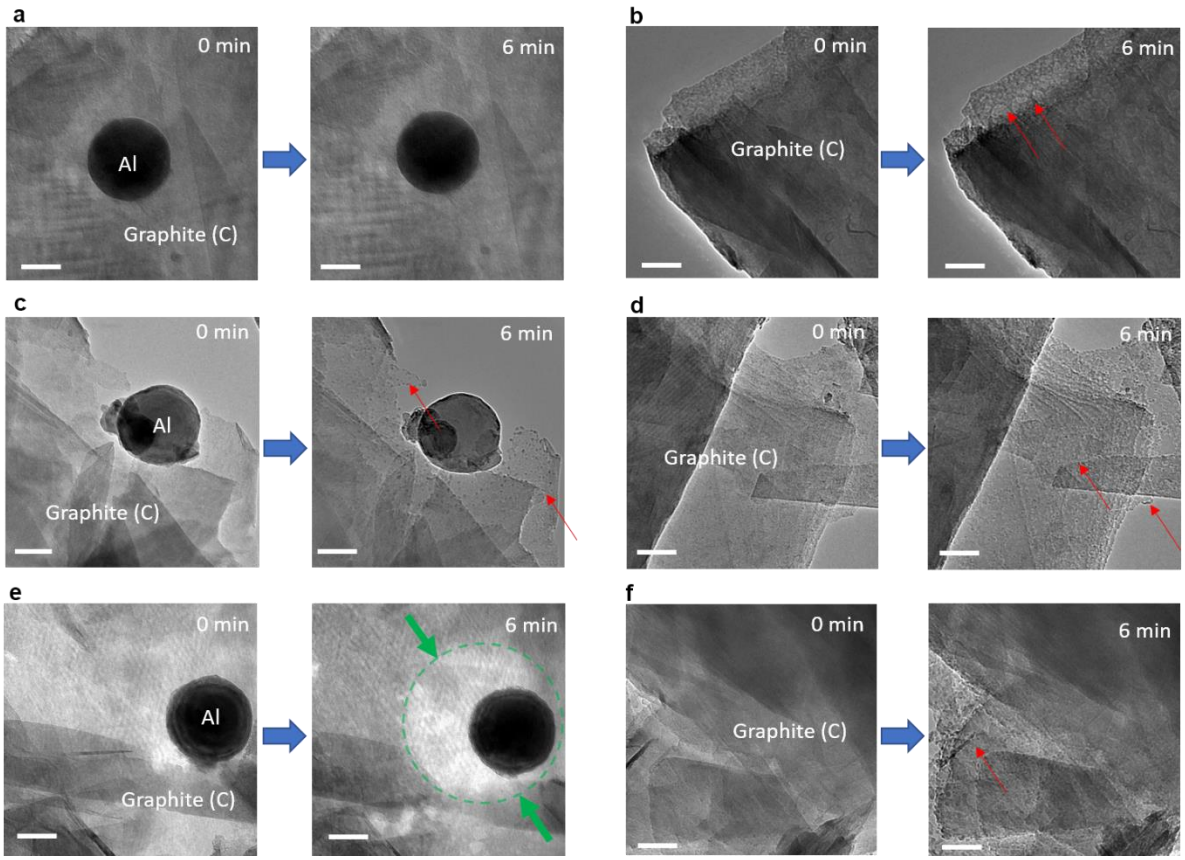

Extended Data Fig. 10 | Illuminating graphite with and without Al nanoparticle in vacuum, N_2 and CO_2. **a-b**, TEM images showing graphite with and without Al nanoparticles before and after ≈ 6 min of electron beam illumination in vacuum (≈ 1×10^{-5} Pa). **c-d**, TEM images showing graphite with and without Al nanoparticles before and after (≈ 6 min of electron beam illumination in N_2 (≈ 50 Pa). **e-f**, TEM images showing graphite with and without Al nanoparticles before and after ≈ 6 min of electron beam illumination in CO_2 (≈ 50 Pa). The electron flux used in all cases is ≈ 9.1×10^{-6} nA·nm^{-2}. No significant etching of graphite in the vicinity of nanoparticle is observed except for the case where the Al is present in a CO_2 environment (marked by green arrows). The etched regions forming 'pits' marked by red arrows in other environments is due to electron beam effect. The scale bars are 100 nm.

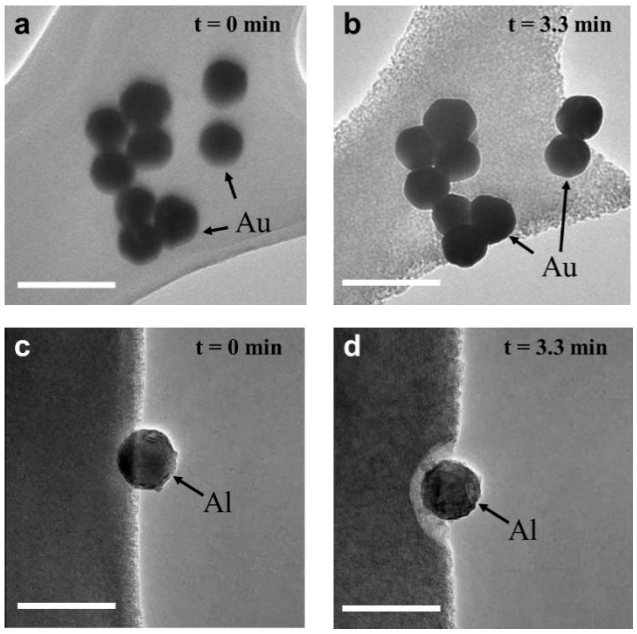

Extended Data Fig. 11 | Etching of carbon with Au and Al nanoparticles in CO_2 under electron beam illumination. a-d, TEM images showing carbon loaded with Au nanoparticles (**a-b**) and, a single Al nanoparticle (**c-d**), before and after ≈ 3.3 min of electron beam illumination in CO_2 (≈ 50 Pa). No preferential etching is observed around the Au nanoparticles despite the uniform damage caused by the electron beam leading to shrinkage of the carbon film (**b**), however, additional preferential etching near the nanoparticle is observed in the case of Al (**d**). The scale bars are 100 nm.

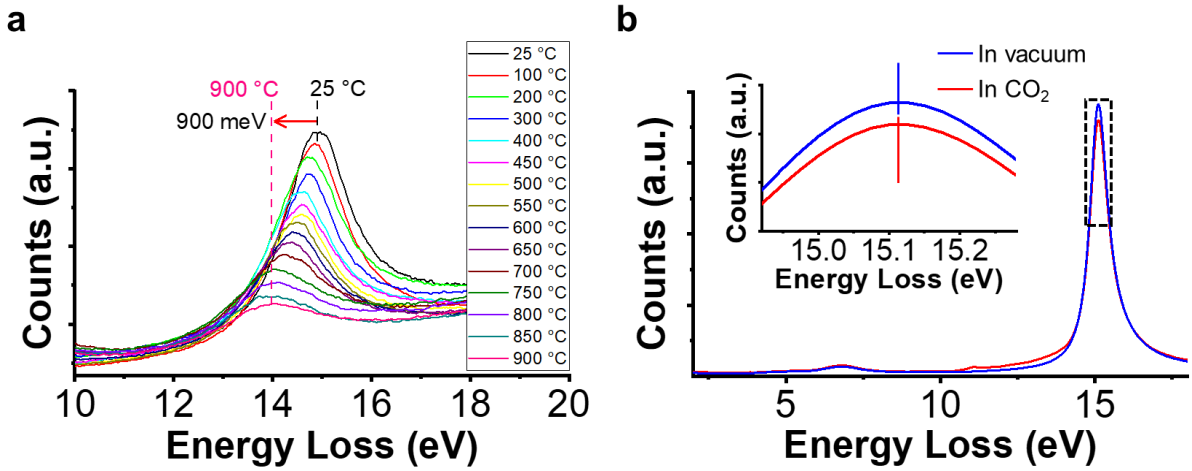

Extended Data Fig. 12 | Temperature measurement during the reverse Boudouard reaction. a, Bulk plasmon peaks of the Al nanoparticle were acquired while intentionally heating the system with a heating holder from room temperature to 900 °C. A total shift of 900 meV was observed between room temperature and 900 °C. **b**, Bulk plasmon peaks of the Al nanoparticle were

acquired both in vacuum and in CO_2. The temperature calculated based on the Al bulk plasmon peak position indicates that the temperature of the nanoparticle remained within the measurement error of ± 5 °C during the reaction. The inset shows the high magnification data from the black dashed box.

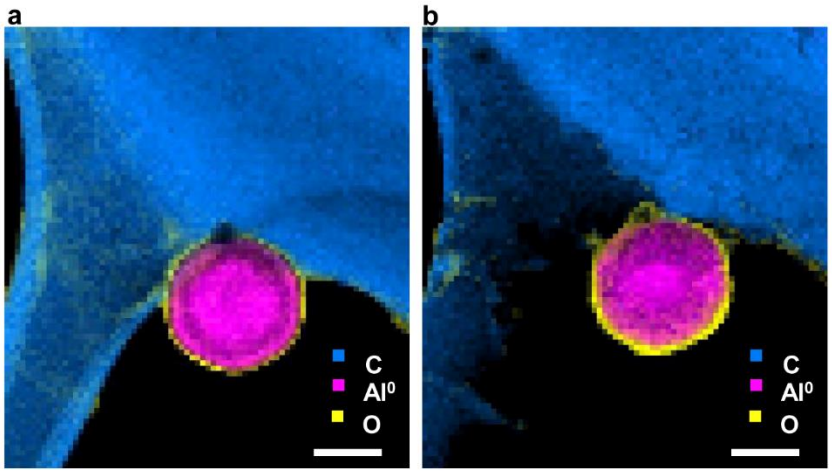

Extended Data Fig. 13 | Measurements of elemental distributions before and after the reverse Boudouard reaction. a, Composite elemental map (carbon: blue; oxygen: yellow; aluminum: magenta) of an Al nanoparticle acquired in vacuum and **b,** acquired in vacuum after electron beam illumination and CO_2 evacuation. Comparison of the composite elemental maps acquired before **a**, and after **b** the reverse Boudouard reaction shows the etching of graphite, and the absence of carbon signal in the nanoparticle. The scale bars are 50 nm.

Extended Data Table 1 | Change of thickness in graphite after electron beam illumination with an electron flux of ≈ 9.1 × 10^{-6} nA·nm^{-2} under different conditions

	With Al nanoparticle			Without Al nanoparticle		
Environment	In vacuum (≈1.2x10^{-5} Pa)	In N_2 (≈50 Pa)	In CO_2 (≈50 Pa)	In vacuum (≈1.2x10^{-5} Pa)	In N_2 (≈50 Pa)	In CO_2 (≈50 Pa)
Thickness change of graphite (nm/min)	1.012 ± 0.584	1.068 ± 0.120	4.310 ± 0.385	0.893 ± 0.433	0.310 ± 0.137	0.642 ± 0.271

The graphite is observed to etch under all conditions, even in ESTEM vacuum without the presence of Al nanoparticles. Under the 50 Pa of CO_2 pressure, the value for the etching of graphite is ≈ 7 times smaller in the absence of Al nanoparticle. The etch rate and the standard deviation is calculated based on at least 3 measured data points. Each data point is acquired from a ≈ 250 nm by ≈ 250 nm area using the quantification method described in the Supplementary Information.

Extended Data Movie 1

Movie showing etching of graphite near the surface of an Al nanoparticle in a CO_2 environment with a pressure of ≈ 50 Pa, illuminated with an electron flux of ≈ 9.1×10^{-6} nA·nm^{-2}. The movie plays at 120 times normal speed. Note the formation of pillar shaped graphite structures due to the uneven etching rate resulting from spatial distribution of electric field around the nanoparticle. The scale bar is 25 nm.